The Astrophysical Journal, 644:914–923, 2006 June 20

VERY LARGE ARRAY H53α AND H92α LINE OBSERVATIONS OF THE CENTRAL REGION OF NGC 253

C. A. Rodríguez-Rico,[1,2] W. M. Goss,[2] J.-H. Zhao,[3] Y. Gómez,[1] and K. R. Anantharamaiah[4,5]

Received 2005 November 14; accepted 2006 February 28

ABSTRACT

We present new VLA observations toward NGC 253 of the recombination line H53α (43 GHz) at an angular resolution of $1\farcs5 \times 1\farcs0$. The free-free emission at 43 GHz is estimated to be $\sim$140 mJy, implying a star formation rate of 2 $M_\odot$ yr^{-1} in the nuclear region of this starburst galaxy. A reanalysis is made for previously reported H92α observations carried out with angular resolution of $1\farcs5 \times 1\farcs0$ and $0\farcs36 \times 0\farcs21$. Based on the line and continuum emission models used for the $1\farcs5 \times 1\farcs0$ angular resolution observations, the RRLs H53α and H92α are tracers of the high-density ($\sim 10^5$ cm^{-3}) and low-density ($\sim 10^3$ cm^{-3}) thermally ionized gas components in NGC 253, respectively. The velocity fields observed in the H53α and H92α lines ($1\farcs5 \times 1\farcs0$) are consistent. The velocity gradient in the central $\sim$18 pc of the NE component, as observed in both the H53α and H92α lines, is in the opposite direction to the velocity gradient determined from the CO observations. The enclosed virial mass, as deduced from the H53α velocity gradient over the NE component, is $\sim 5 \times 10^6$ $M_\odot$ in the central $\sim$18 pc region. The H92α line observations at high angular resolution ($0\farcs36 \times 0\farcs21$) reveal a larger velocity gradient, along a P.A. $\sim -45^\circ$ on the NE component, of $\sim$110 km s^{-1} arcsec^{-1}. The dynamical mass estimated using the high angular resolution H92α data ($\sim 7 \times 10^6$ $M_\odot$) supports the existence of an accreted massive object in the nuclear region of NGC 253.

Subject heading: galaxies: starburst

1. INTRODUCTION

NGC 253 is one of the nearest ($\sim$2.5 Mpc) and brightest starburst galaxies, cataloged as an SAB(s)c galaxy (de Vaucouleurs et al. 1976). This galaxy has an inclination of $\sim 79^\circ$ with respect to the line of sight with major axis located at a position angle (P.A.) of 51°, also containing a barlike feature tilted by 18° with respect to the major axis (Pence 1981). Observations of NGC 253 have been carried out in the radio (Turner & Ho 1985; Ulvestad & Antonucci 1997; Mohan et al. 2002, 2005; Boomsma et al. 2005), infrared (Engelbracht et al. 1998), optical (Forbes et al. 2000; Arnaboldi et al. 1995), and X-ray (Weaver et al. 2002) wavelengths. Radio observations, which are not affected by dust absorption, are an excellent tool to study the structure and kinematics of the nuclear region of NGC 253. Observations in the 21 cm line (Boomsma et al. 2005) reveal extraplanar motions of H I that occur at a large scale of up to 12 kpc. High angular resolution radio continuum observations (Ulvestad & Antonucci 1997) have revealed a number (>60) of compact sources in the central 300 pc of this galaxy, supporting the scenario of a massive star formation episode occurring in the center of NGC 253. Nearly half of these compact continuum sources are dominated by thermal radio emission from H II regions (Turner & Ho 1985; Antonucci & Ulvestad 1988; Ulvestad & Antonucci 1997). The radio continuum and radio recombination line (RRL) emission, observed at high angular resolution, have been modeled using different density components for the ionized gas (Mohan et al. 2005). The emission models suggest the existence of both low- ($\sim 10^3$ cm^{-3}) and high-density (>10^4 cm^{-3}) ionized gas in the central region of NGC 253. On the other hand, the most luminous source (5.79-0.39) is unresolved (<1 pc) at 22 GHz, suggesting the existence of an active galactic nucleus (AGN) in the center of this galaxy (Ulvestad & Antonucci 1997). Observations of broad H_2O maser line emission ($\geq$100 km s^{-1}) near this radio continuum source have been invoked as further evidence of the presence of a massive object in NGC 253 (Nakai et al. 1995). Mohan et al. (2002) modeled the VLA continuum and RRL emission for the nuclear region of NGC 253 and favor an AGN as the source responsible for the ionization. Observations of hard X-ray emission toward the core of NGC 253 were also interpreted as evidence of AGN activity (Weaver et al. 2002).

The barlike structure was first observed toward NGC 253 in the near-infrared (NIR), covering the inner 150″ region of the galaxy (Scoville et al. 1985; Forbes & Depoy 1992). The existence of the stellar bar is supported by the observed morphology at optical and mid-infrared frequencies (Forbes & Depoy 1992; Piña et al. 1992). A counterpart of the stellar bar in NGC 253 has been found in CO (Canzian et al. 1988), HCN (Paglione et al. 1995), and CS (Peng et al. 1996). Observations in the RRL H92α (Anantharamaiah & Goss 1996) at an angular resolution of $1\farcs8 \times 1\farcs0$ reveal a velocity field that is discrepant with the CO, CS, and HCN observations. Anantharamaiah & Goss (1996) proposed that the kinematics observed in the H92α could result from a merger of two counterrotating disks. The observed H92α and CO line velocity fields were modeled by Das et al. (2001) using a barlike potential for NGC 253, which is in reasonable agreement with the observed H92α line velocity field. However, this kinematical model can only reproduce the velocity field of the CO and CS and does not agree with the H92α RRL observations. Based on the discrepancy of the CO and the ionized gas kinematics, Das et al. (2001) proposed that the accretion of a compact object ($\sim 10^6$ $M_\odot$) about 10^7 years ago could account for the velocity field observed in the H92α RRL. Paglione et al. (2004) observed the CO emission at 3″ angular resolution for the inner region and modeled the kinematics of the molecular gas

[1] Centro de Radioastronomía y Astrofísica, Universidad Nacional Autonoma de México, Campus Morelia, Apartado Postal 3-72, Morelia, Michoacán 58089, México; c.rodriguez@astrosmo.unam.mx, y.gomez@astrosmo.unam.mx.

[2] National Radio Astronomy Observatory, P.O. Box O, 1003 Lopezville Road, Socorro, NM 87801; mgoss@nrao.edu.

[3] Harvard-Smithsonian Center for Astrophysics, 60 Garden Street, Cambridge, MA 02138; jzhao@cfa.harvard.edu.

[4] Raman Research Institute, CV Raman Avenue, Sadashivanagar PO, Bangalore 560-080, India.

[5] Deceased 2001 October 29.

using a bar potential, concluding that motions of the CO gas in the central 150 pc are consistent with a bar potential and reporting evidence of the existence of an inner Lindblad resonance (ILR).

Previous interferometric observations of RRLs have been made at low frequencies (e.g., ~8.3 GHz, H92α). VLA observations at $1\farcs5 \times 1\farcs0$ angular resolution were used by Anantharamaiah & Goss (1996) to study the kinematics of NGC 253; Mohan et al. (2002, 2005) used the VLA observations at $1\farcs5 \times 1\farcs0$ and $0\farcs3$ angular resolutions to determine the physical properties of the ionized gas in NGC 253. In this paper we analyze the kinematics of the ionized gas in the nuclear region of NGC 253 using high-frequency RRL observations (~43 GHz) and the high angular resolution observations (at $0\farcs3$) in the RRL H92α. Also we use the VLA observations in the RRL H53α and the 43 GHz radio continuum, along with previously reported H92α line and 8.3 GHz radio continuum observations (Mohan et al. 2005), in order to estimate the physical properties of the ionized gas. This paper is complementary to the results summarized by Mohan et al. (2005). In § 2 we present the observations and data reduction, while in § 3 we present the results for the H53α and H92α RRLs. In § 4.1 a model for the emission of the RRLs H53α and H92α, as well as for the radio continuum at 43 and 8.3 GHz, is presented. In § 4.2 we analyze the kinematics for the ionized gas in the center of NGC 253, and in § 5 we present the conclusions.

2. VLA OBSERVATIONS

2.1. H53α *Line*

The H53α line ($\nu_{\rm rest}$ = 43309.4 MHz) was observed in the CnD configuration of the VLA on 2003 January 18, 19, and 20. We used cycles with integration times of 10 minutes on NGC 253 and 1 minute on the phase calibrator J0120−270 (~0.7 Jy). Four frequency windows (LOs) were used to observe the RRL H53α, centered at 42885.1, 42914.9, 42935.1, and 42964.9 GHz. For each frequency window, the on-source integration time was ~2 hr, using the mode of 15 spectral channels with a channel separation of 3.125 MHz (~22 km s^{-1}). The data calibration was carried out for each frequency window using the continuum channel, consisting of the central 75% of the band. The flux density scales were determined from observations of J0137+331 (3C 48; 0.54 Jy). The bandpass response of the instrument was corrected using observations of J0319+415 (3C 84; ~7.5 Jy). The parameters of the observations are summarized in Table 1. In order to track reliably the phase variations introduced by the troposphere, the calibration of the data was performed correcting for the phases in a first step and subsequently correcting for both amplitude and phase. The line data were further calibrated using the solutions obtained by self-calibrating the continuum channel of each frequency window. The radio continuum images were obtained by combining the continuum channels of each frequency window using the task DBCON from AIPS, and the self-calibration method was also applied to these combined data. The H53α line cubes and the 43 GHz continuum image were made using a natural weighting scheme and then convolved to obtain a Gaussian beam of $1\farcs5 \times 1\farcs0$ (P.A. = 0°). The combination of the different frequency windows was made following a similar method to that used for the H53α line observed toward M82 (Rodríguez-Rico et al. 2004): (1) the line data from each frequency window were regridded in frequency using the GIPSY reduction package; (2) before combining the four LOs into a single line cube, the continuum emission was subtracted for each frequency window using the AIPS task IMLIN with a zero-order polynomial fit based on the line free channels; and (3) the four line cubes (after subtraction of the continuum) were combined into a single line cube. The total line bandwidth, after combining all of the windows, is about 150 MHz (1000 km s^{-1}). The line data cube was Hanning smoothed using the task XSMTH in AIPS to reduce the Gibbs effect, and the final velocity resolution is ~44 km s^{-1}.

TABLE 1
OBSERVING PARAMETERS FOR NGC 253 USING THE VLA

Parameter	H53α RRL (43 GHz)
Right ascension (J2000.0)	$00^{\rm h}47^{\rm m}33\fs18$
Declination (J2000.0)	$-25°17'17\farcs0$
Angular resolution continuum	$1\farcs5 \times 1\farcs0$, P.A. = 0°
Angular resolution line	$1\farcs5 \times 1\farcs0$, P.A. = 0°
On-source observing duration	8 hr
Bandwidth	125 MHz
Number of spectral channels	38
Center $V_{\rm hel}$	200 km s^{-1}
Velocity coverage	1000 km s^{-1}
Velocity resolution	44 km s^{-1}
Amplitude calibrator	J0137+331
Phase calibrator	J0120−270
Bandpass calibrator	J0319+415
rms line noise per channel	0.65 mJy beam^{-1}
rms, continuum	0.2 mJy beam^{-1}

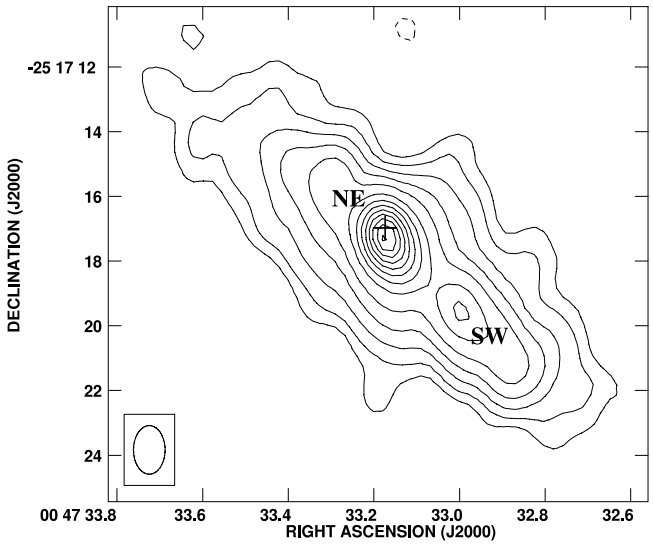

FIG. 1.—Radio continuum image of NGC 253 at 43 GHz obtained using the VLA. Contour levels are drawn at −3, 3, 6, 12, 24, 48, 96, 144, 192, 240, 288, 336, 384, and 432 times the rms of 0.2 mJy beam^{-1}. The plus sign shows the position of the compact source 5.79-39.0 (Ulvestad & Antonucci 1997). The angular resolution is $1\farcs5 \times 1\farcs0$, P.A. = 0°.

2.2. H92α *Line*

We also present previously reported observations of the RRL H92α ($\nu_{\rm rest}$ = 8309.4 MHz) at $1\farcs5 \times 1\farcs0$, P.A. = 0° (Anantharamaiah & Goss 1996) and $0\farcs36 \times 0\farcs21$, P.A. = −3° (Mohan et al. 2002, 2005) angular resolutions toward NGC 253. The H92α RRL images at $1\farcs5 \times 1\farcs0$ angular resolution were produced by combining observations carried out in the B (1990 August 31 and September 1), C (1988 May 14 and 23), and D (1988 July 1 and 19) configurations of the VLA. In order to obtain the same half-power full width (HPFW) beam as the H53α line cube, the H92α line cube was made using these "B+C+D" combined data applying a natural weighting scheme. Anantharamaiah & Goss (1996) have already used these B+C+D combined observations to analyze the kinematics of the ionized

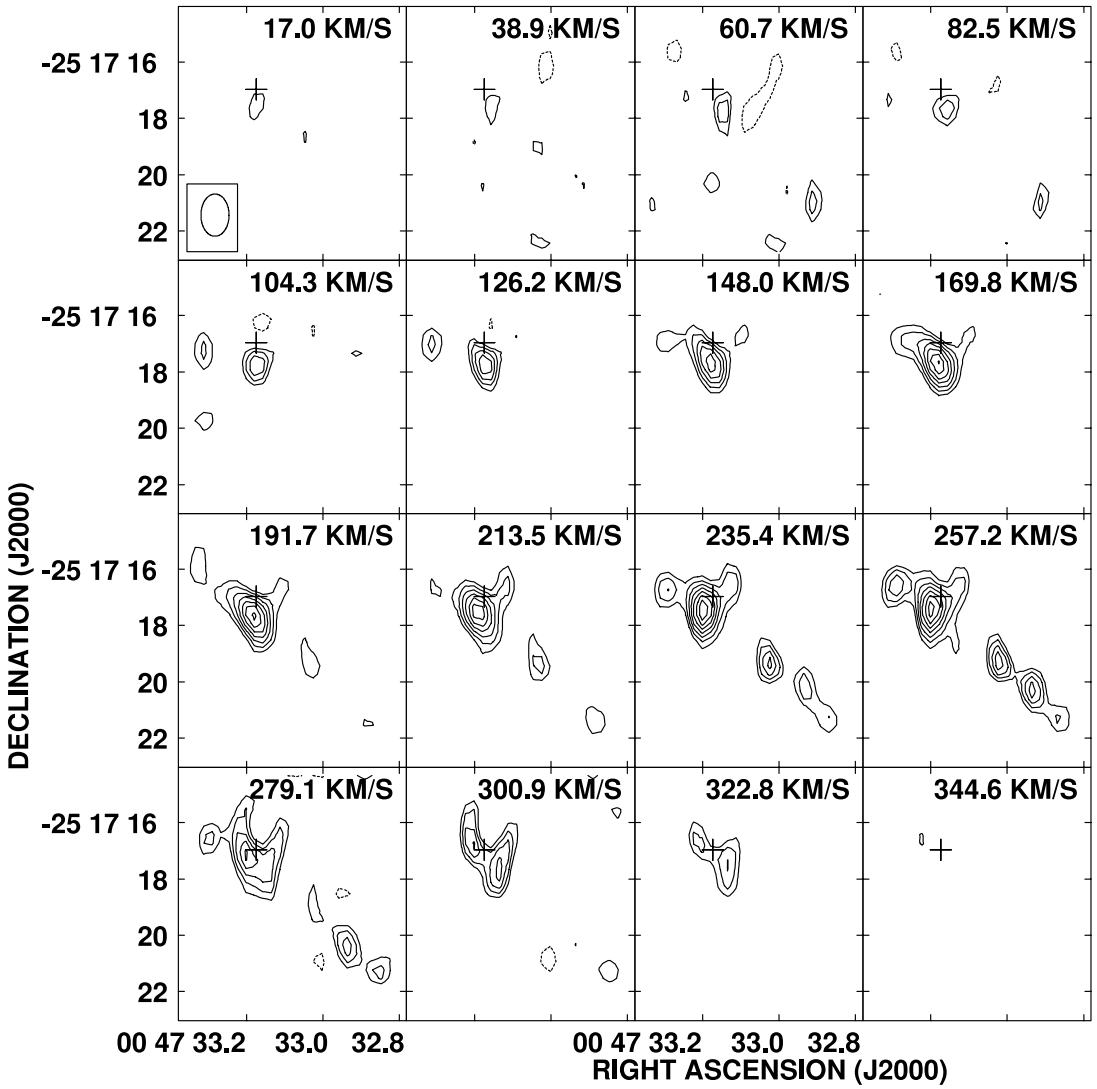

FIG. 2.—Channel images of the H53α line emission toward NGC 253 obtained using the VLA. Contours are -3, 3, 4, 5, 6, 7, 8, 9, and 10 times 0.65 mJy beam^{-1}, the rms noise. The plus sign shows the position of the compact source 5.79-39.0 (Ulvestad & Antonucci 1997). The synthesized beam ($1\farcs5 \times 1\farcs0$ FWHM, P.A. $= 0^\circ$) is shown in the first panel. The central heliocentric velocity is given above for each image.

gas in the central $10''$ of NGC 253 with an angular resolution of $1\farcs8 \times 1\farcs0$, P.A. $= 10^\circ$. The higher angular resolution ($0\farcs36 \times 0\farcs21$, P.A. $= -3^\circ$) observations of the H92α line toward NGC 253 were made with the VLA in the A configuration (1999 July 9 and 12) and have been previously reported by Mohan et al. (2002). Recently, Mohan et al. (2005) used these H92α data along with observations in the H75α and H166α data to model the RRL and the radio continuum emission in order to determine the physical parameters of the ionized gas. In this paper we use these high angular resolution observations to study the kinematics of the ionized gas in the nuclear $5''$ region of NGC 253. Because of the different spectral line grid of the H92α high angular resolution observations and the H92α B+C+D data, a combined data set "A+B+C+D" was not produced.

For the H92α line observations, the phase calibrator was J0118$-$216 and the bandpass calibrator was J2253+161. A spectral mode with 31 channels was used. The continuum images were obtained by averaging the data in the central 75% of the total band. The continuum data were processed using standard calibration and self-calibration procedures. The calibration and self-calibration used for the continuum data were then applied to the line data. All of the images were made in the AIPS environment. The line images were Hanning smoothed to reduce the Gibbs effect, and the velocity resolution is 56.4 km s^{-1}. Further observational details are summarized by Mohan et al. (2002, 2005).

3. RESULTS

Figure 1 shows the radio continuum emission of NGC 253 at 43 GHz with an angular resolution of $1\farcs5 \times 1\farcs0$, P.A. $= 0^\circ$ ($1'' \simeq 12$ pc). The integrated 43 GHz continuum flux density is 360 ± 20 mJy, obtained by integrating the flux density over the nuclear $30''$ region using the task IRING in AIPS. The radio continuum image at 43 GHz shows two radio continuum components, NE and SW, in addition to extended emission (see Fig. 1). The continuum peak position of the NE component, α(J2000.0) $= 00^{\rm h}47^{\rm m}33\fs17 \pm 0\fs01$, δ(J2000.0) $= -25^\circ 17' 17\farcs4 \pm 0\farcs1$, coincides within $0\farcs2$ with the position of the compact source 5.79-39.0 (Ulvestad & Antonucci 1997).

Figure 2 shows the H53α velocity channel images of NGC 253 with an angular resolution of $1\farcs5 \times 1\farcs0$ (P.A. $= 0^\circ$). The H53α line emission is detected toward both the NE and SW continuum components above a 3 σ level ($\sim$2 mJy). The ionized gas is observed in the H53α line at heliocentric velocities that range from

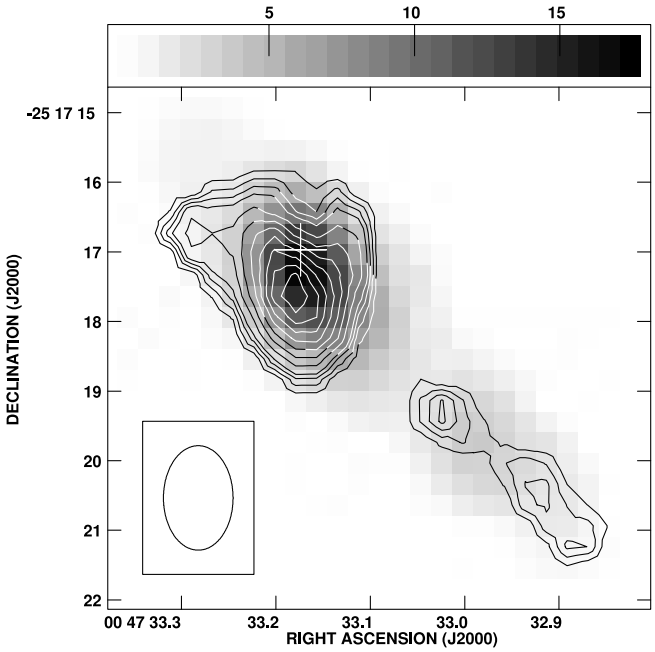

FIG. 3.—Velocity-integrated (moment 0) H53α line emission (*contours*) superposed on the moment 0 of the H92α line emission (*gray scale*) toward NGC 253. Contour levels are drawn at 5%, 10%, 15%, 20%, 30%, . . . , 90% the peak line emission of 1.16 Jy beam^{-1} km s^{-1}. The gray scale (moment 0 of H92α) covers the range 0.18–18 Jy beam^{-1} km s^{-1}. The plus sign shows the position of the compact source 5.79-39.0 (Ulvestad & Antonucci 1997). The HPFW, for both the H53α and H92α line images, is $1\farcs5 \times 1\farcs0$, P.A. $= 0^\circ$.

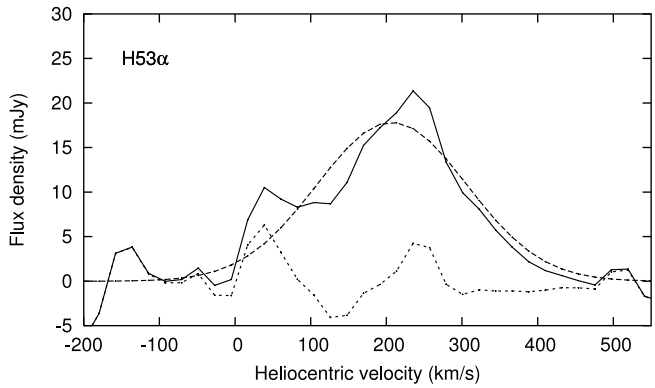

FIG. 4.—Total integrated H53α spectrum from NGC 253, obtained by integrating over the central 10″. The solid line shows the data, the dashed line shows the Gaussian fit, and the dot-dashed line shows the residuals to this fit.

17 to 345 km s^{-1}. The velocity-integrated H53α line emission (moment 0) is shown in Figure 3 superposed on the moment 0 of the H92α line. There is good correspondence between the integrated line emission of the RRLs H53α and H92α. In addition, the peak position of the integrated H53α line emission is in agreement with the peak position of the 43 GHz radio continuum image. In the H53α line images, both the NE and SW components are spatially resolved only along the major axis.

Figure 4 shows the H53α line spectrum integrated over the central 10″ region of NGC 253. By fitting a Gaussian, the estimated central heliocentric velocity is 210 ± 10 km s^{-1}, the FWHM of the line is 230 ± 20 km s^{-1}, and the peak line flux density is 21 ± 2 mJy. The resulting fit is shown in Figure 4 along with the residuals to the fit. The central velocity is in agreement with previous estimates in the optical (225 ± 5 km s^{-1}; Arnaboldi et al. 1995) and IR (230 ± 10 km s^{-1}; Prada et al. 1998). The velocity-integrated H53α line flux density determined from our observations is $(0.69 \pm 0.09) \times 10^{-20}$ W m^{-2}, in agreement with the previous measurement of $(0.94 \pm 0.38) \times 10^{-20}$ W m^{-2} derived from single-dish observations (Puxley et al. 1997). A Gaussian function was also used to determine the characteristics of the spectra obtained by integrating over the NE and SW regions. Table 2 lists the results for the total integrated H53α line emission profile, as well as for profiles that correspond to the NE and SW components. The values listed for the H53α line are peak flux density S_L, FWHM, the heliocentric velocity $V_{\rm hel}$, and the velocity-integrated H53α line emission.

Figure 5 shows the velocity field (moment 1) of the H53α line at an angular resolution of $1\farcs5 \times 1\farcs0$ (P.A. $= 0^\circ$). Figure 6 shows the H92α velocity field made using the B+C+D data of Anantharamaiah & Goss (1996) at the same angular resolution. The velocity field of the ionized gas as observed in the H53α line agrees with observations of the RRL H92α (see § 4.2 for a detailed comparison). In the NE component of NGC 253 the redshifted gas is observed toward the northwest and the blueshifted gas toward the southeast. In the region located south of the radio continuum peak, there is a blueshifted component that is more apparent in the H53α line than in the H92α line. A detailed comparison between the line profiles of H53α and H92α in this region shows that the H53α line is broader than the H92α line by $\sim$50 km s^{-1} and there is a relative velocity shift between these two RRLs of $\sim$30 km s^{-1}. In the elongated SW component, the redshifted gas is located at the southwest and the blueshifted gas is at the northeast. The velocity gradient was measured, at $1\farcs5 \times 1\farcs0$ angular resolution, along the major (P.A. $= 52^\circ$) and nearly along the minor (P.A. $= -45^\circ$) axis for both RRLs H53α and H92α. The H53α velocity gradient along the major axis of NGC 253 (measured over the NE component) is 12 ± 3 km s^{-1} arcsec^{-1}, comparable to the corresponding H92α velocity gradient ($\sim$11 km s^{-1} arcsec^{-1}). The velocity gradients measured in the RRLs H53α and H92α (both at $1\farcs5 \times 1\farcs0$) along the P.A. $= -45^\circ$ are 42 ± 8 and 24 ± 2 km s^{-1} arcsec^{-1}, respectively.

Figure 7 shows the H92α velocity field at an angular resolution of $0\farcs36 \times 0\farcs21$ (P.A. $= -3^\circ$). At this angular resolution, the H92α line emission is detected only toward the NE component with an angular size of $\sim$0.″6 (7 pc). Based on these H92α data, a larger velocity gradient of 110 ± 20 km s^{-1} arcsec^{-1} is measured along a P.A. $\simeq -45^\circ$. This velocity gradient is about a factor of 4 larger than the velocity gradient estimated using the lower angular resolution H92α observations ($1\farcs5 \times 1\farcs0$). The lower velocity gradient measured in the low angular resolution image of H92α ($1\farcs5 \times 1\farcs0$) is due to a beam dilution effect. By convolving the high angular resolution data of H92α with a Gaussian beam of $1\farcs5 \times 1\farcs0$ angular resolution, the velocity gradient measured along the P.A. $= -45^\circ$ is consistent with the lower angular resolution H92α data.

4. DISCUSSION

4.1. *Models for the Radio Continuum and Recombination Line Emission*

In Table 3 we summarize the 43 GHz continuum flux density measurement along with previous measurements (5–300 GHz) for the central 30″ region of NGC 253. These flux density values have been used to determine the relative contributions from free-free, synchrotron, and dust emission. At frequencies $<$50 GHz, the relative contributions of free-free and nonthermal emission

TABLE 2
H53α AND H92α LINE PARAMETERS FOR NGC 253

	H53α					H92α				
FEATURE	S_{C43}[a] (mJy)	S_L (mJy)	$\Delta V_{\rm FWHM}$ (km s^{-1})	$V_{\rm hel}$ (km s^{-1})	$S_L\Delta V_{\rm FWHM}$ (10^{-20} W m^{-2})	$S_{C8.3}$[a] (mJy)	S_L (mJy)	ΔV (km s^{-1})	$V_{\rm hel}$ (km s^{-1})	$S_L\Delta V_{\rm FWHM}$ (10^{-22} W m^{-2})
NGC 253 NE	134 ± 5	9.0 ± 0.5	200 ± 10	220 ± 5	0.25 ± 0.01	278 ± 10	4.5 ± 0.1	190 ± 5	200 ± 2	2.4 ± 0.2
NGC 253 SW	24 ± 2	2.8 ± 0.3	130 ± 20	215 ± 10	0.04 ± 0.01	40 ± 4	0.7 ± 0.1	160 ± 15	220 ± 10	0.3 ± 0.03
NGC 253 total	360 ± 20	21 ± 2	230 ± 20	210 ± 10	0.69 ± 0.09	605 ± 10	9.0 ± 0.5	190 ± 10	206 ± 4	4.7 ± 0.5

[a] Continuum emission was obtained by integrating over the region where both RRLs H53α and H92α were detected.

are dominant compared to the thermal dust emission. However, at frequencies >50 GHz, the dust contribution is more significant. The estimated contribution of the thermal free-free emission at 43 GHz is ~140 mJy, while the nonthermal emission accounts for ~220 mJy. These values were obtained assuming that the thermal continuum free-free flux density shows $S_{\rm ff}(\nu) \propto \nu^{-0.1}$. Using the observed flux density measurements of the radio continuum in the range of 5–98 GHz, and following the procedure used by Turner & Ho (1983), the spectral index for the nonthermal emission is $\alpha_{\rm synchrotron} = -0.73 \pm 0.06$. After subtracting the free-free and nonthermal emission from the total continuum emission over the 5–300 GHz frequency range, we obtain the spectral index value for the dust emission $\alpha_{\rm dust} = 3.9 \pm 0.2$. Figure 8 shows the contribution from thermal free-free, synchrotron, and thermal dust emission along with the total radio continuum over the frequency range 5–300 GHz. The thermal free-free radio continuum flux density at 43 GHz may be used to estimate the ionization rate ($N_{\rm Lyc}$) from NGC 253 using (Schraml & Mezger 1969; Rodríguez et al. 1980)

$$\frac{N_{\rm Lyc}}{\rm s^{-1}} = 9.0\times10^{43}\left(\frac{S_{C,\rm th}}{\rm mJy}\right)\left(\frac{T_e}{10^4\ \rm K}\right)^{0.35}\left(\frac{\nu}{4.9\ \rm GHz}\right)^{0.1}\left(\frac{D}{\rm kpc}\right)^2, \quad (1)$$

where T_e is the electron temperature, ν is the frequency, and D is the distance to NGC 253. The estimated ionizing flux at 43 GHz, assuming $T_e = 10^4$ K and $D = 2.5$ Mpc, is $\sim 7\times10^{52}$ s^{-1}. This $N_{\rm Lyc}$ value is a factor of ~5 lower than that estimated by Puxley et al. (1997), using the H40α line flux density and assuming local thermodynamic equilibrium (LTE). However, the RRL H40α line emission mainly arises from stimulated emission, implying a smaller value of the star formation rate (SFR). On the other hand, the SFR ($\Psi_{\rm OB}$) can also be estimated using the relation $N_{\rm Lyc} = 5.4\times10^{52}\Psi_{\rm OB}$ s^{-1} (Anantharamaiah et al. 2000), obtained assuming a mass range of 1–100 $M_\odot$ in the Miller-Scalo initial mass function (IMF). The total SFR derived in the nuclear regions of NGC 253 is thus 2 $M_\odot$ yr^{-1}.

The emission in the RRLs H53α and H92α, as well as the radio continuum at 43 and 8.3 GHz, was modeled for the two continuum components (NE and SW) of NGC 253 observed at an angular resolution of $1\farcs5\times1\farcs0$ (P.A. = 0°). The line and continuum flux densities were measured over regions where both H92α and H53α are detected. The models consist of a collection of two families of H II regions, each with different electron densities. The electron density ranges that were explored are $n_e = 10^2$–10^4 and

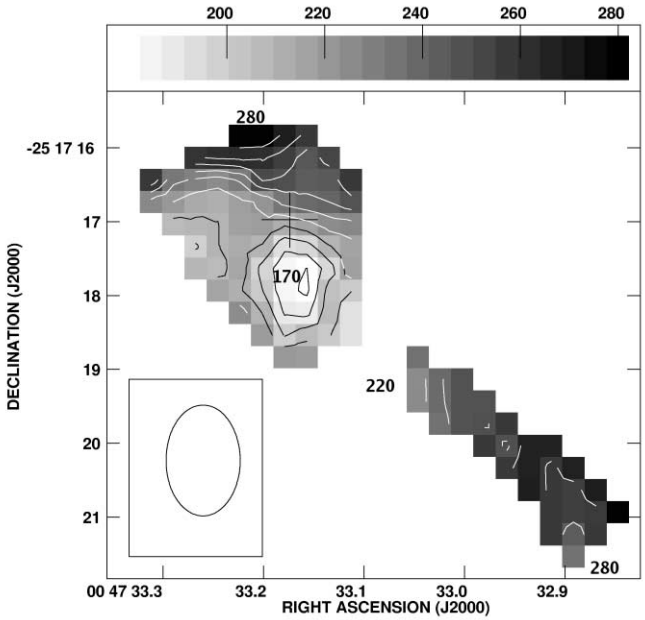

FIG. 5.—Velocity field observed in the H53α line from NGC 253. Contour levels are the heliocentric velocities at 180, 190, 200, 210, 220, 230, 240, 250, 260, and 270 km s^{-1}. The gray scale ranges from 170 to 280 km s^{-1}. The plus sign shows the position of the compact source 5.79-39.0 (Ulvestad & Antonucci 1997). The HPFW is $1\farcs5\times1\farcs0$, P.A. = 0°.

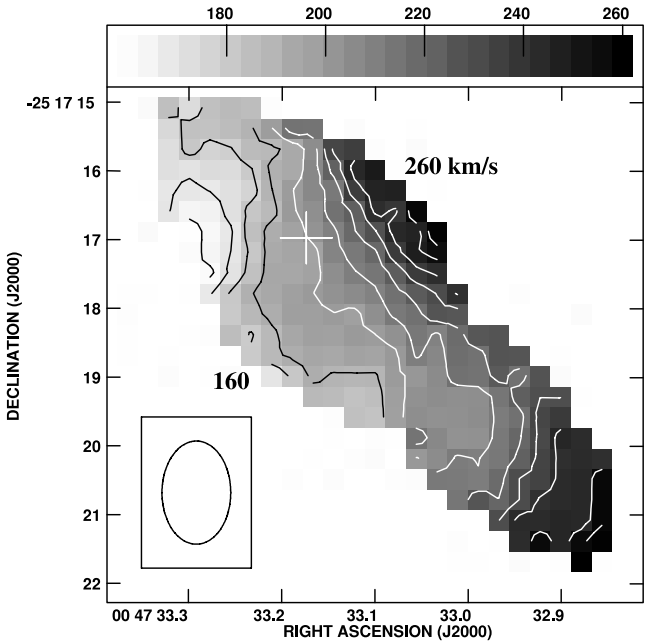

FIG. 6.—H92α velocity field of NGC 253 (Anantharamaiah & Goss 1996), shown in contours superposed on the gray-scale image of the same H92α velocity field. Contour levels are drawn for the heliocentric velocities of the ionized gas from 160 to 260 km s^{-1} in steps of 10 km s^{-1}, and the gray scale covers the same heliocentric velocity range. The plus sign shows the position of the compact source 5.79-39.0 (Ulvestad & Antonucci 1997). The HPFW is $1\farcs5\times1\farcs0$, P.A. = 0°.

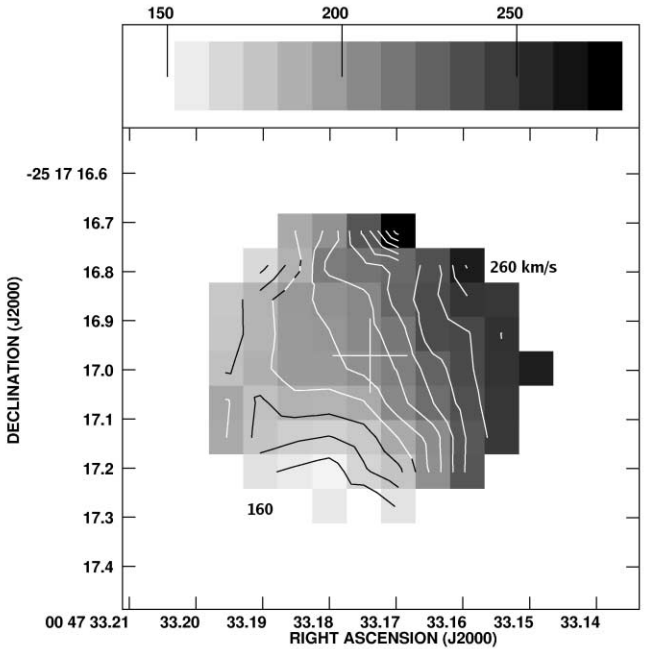

FIG. 7.—High angular resolution ($0\farcs36 \times 0\farcs21$, P.A. $= -3^\circ$) heliocentric velocity field (moment 1) image of the H92α line emission toward NGC 253 obtained using the VLA A configuration data. Contour levels are drawn at 160, 170, . . . , 260 km s^{-1}. The plus sign shows the position of the compact source 5.79-39.0 (Ulvestad & Antonucci 1997).

10^4–10^7 cm^{-3} for the low- and high-density gas components, respectively. The contribution from nonthermal synchrotron emission that arises from supernova remnants and the possible AGN and free-free emission from H II regions were also considered. The RRL emission has been computed considering that the population of the atomic levels deviates from LTE. The non-LTE effects result in both internally and externally stimulated line emission. The formalism used to compute the RRL and radio continuum flux densities at each frequency follows that used by Rodríguez-Rico et al. (2004). In these models, the electron density (n_e), temperature (T_e), size (s_o), and the number of H II regions ($N_{\rm H\,II}$) are free parameters. In order to reduce the number of free parameters, the size of each H II region has been assumed to be a function of the electron density and the number of ionizing photons emitted by the embedded O star by $s_o n_e^{2/3} = U$, where U is a function of the spectral type of the star (Panagia 1973). In these models, early-type O7 stars have been used as the source of the ionizing continuum flux for each H II region. The results obtained for n_e and $N_{\rm H\,II}$ were constrained by the observed line and continuum flux densities, as well as the volume of the total line emission, assuming spherical H II regions.

TABLE 3
OBSERVED CONTINUUM FLUX DENSITIES FOR NGC 253

Frequency (GHz)	Flux Density (mJy)
5	1400 ± 70[a]
8.3	1100 ± 25[b]
15	640 ± 30[a]
43	360 ± 20[c]
85	350 ± 50[d]
99	320 ± 30[e]
230	1700 ± 200[f]
300	4400 ± 1700[g]

NOTE.—Integrated flux density measured over the inner $\sim$30″ region.
[a] Turner & Ho (1983).
[b] Mohan et al. (2002).
[c] This work.
[d] Carlstrom (1990).
[e] Peng et al. (1996).
[f] Krugel et al. (1990).
[g] Chini et al. (1984).

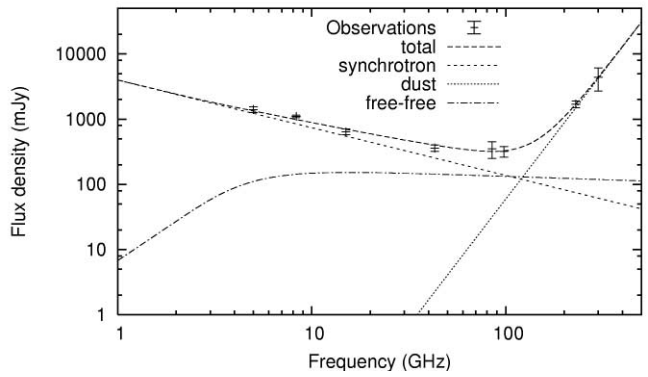

FIG. 8.—Integrated radio continuum emission measured toward the nuclear 30″ region of NGC 253 at 5, 15 (Turner & Ho 1983), 43 (this work), 85 (Carlstrom 1990), 98 (Peng et al. 1996), 230 (Krugel et al. 1990), and 300 GHz (Chini et al. 1984). The contributions to the continuum flux density are free-free ($S_{\rm ff} \propto \nu^{-0.1}$), synchrotron ($S_{\rm synchrotron} \propto \nu^{-0.7}$), and dust ($S_{\rm dust} \propto \nu^{3.9}$) emission, which are shown as indicated.

The models suggest that the thermally ionized gas in the NE component consists of a collection of extended ($\sim$1–4 pc) low-density ($\sim 10^2$–10^3 cm^{-3}) H II regions and compact ($\sim$0.01–0.06 pc) high-density ($\sim 10^5$–10^6 cm^{-3}) H II regions. In order to reproduce the observations, the mass of ionized gas in the low-density component must be a factor of $\sim 10^3$ larger than the mass of ionized gas in the high-density component. The ionized gas in the SW component also consists of low- and high-density H II regions, characterized by $n_e \simeq 10^2$ and 10^5–10^6 cm^{-3}, respectively. Table 4 lists the physical parameters of these H II regions: the electron temperature (T_e), electron density (n_e), size, emission measure (EM), mass of ionized gas, continuum optical depth (τ_c) at 8.3 and 43 GHz, departure coefficients [b_n and $\beta_n = 1 - (kT_e/h\nu_L)d \ln b_n/dn$, where n is the quantum number] for the H53α and H92α RRLs, the contribution of free-free emission, and the Lyman continuum photon rate. The second and third columns list these parameters for the low- and high-density H II regions on the NE component. The fourth and fifth columns list the corresponding parameters for the SW component. Based on these models, the RRL H92α arises mainly as externally stimulated line emission from the extended low-density ($\sim 10^3$ cm^{-3}) H II regions, with $\beta_n < -20$.

The thermal free-free contribution from both the low- and high-density component to the total observed continuum emission ranges from $\sim$30% to $\sim$80%. The total mass of thermally ionized gas in each component (NE and SW) is $\sim 10^3\ M_\odot$. The Lyman continuum emission rate of 5.9×10^{52} s^{-1} obtained from the RRL emission models (see Table 4) is consistent with 7×10^{52} s^{-1}, obtained from the continuum emission models (shown in Fig. 8). The Lyman continuum emission rates for the NE and SW components (listed in Table 4) were obtained only for regions where H53α line emission was detected. On the other hand, the value of 7×10^{52} s^{-1} was estimated by integrating over the central 30″ region, which explains the slightly different results.

TABLE 4
RESULTS FROM MODELS USING A COLLECTION OF H II REGIONS FOR NGC 253

PARAMETER	NE REGION		SW REGION	
	Low Density[a]	High Density[a]	Low Density[a]	High Density[a]
T_e (K)	7500 ± 2500	7500 ± 2500	5000 ± 1000	5000 ± 1000
n_e (cm^{-3})	(1.6 ± 1.4) × 10^3	(5.5 ± 4.5) × 10^5	200 ± 100	(6.5 ± 3.5) × 10^5
Size (pc)	2.4 ± 1.7	0.04 ± 0.03	4.5 ± 1.5	0.02 ± 0.01
EM (cm^{-6} pc)	(3 ± 2) × 10^6	(50 ± 45) × 10^8	(1.5 ± 1) × 10^5	(6 ± 4) × 10^9
$M_{\rm H\,II}$ ($M_\odot$)	(3 ± 2) × 10^3	7 ± 6	(5 ± 3) × 10^3	0.4 ± 0.3
τ_C (8.3 GHz)	(6 ± 5) × 10^{-3}	32 ± 30	(6 ± 5) × 10^{-4}	60 ± 40
τ_C (43 GHz)	(6 ± 5) × 10^{-5}	1.0 ± 0.9	(4 ± 3) × 10^{-5}	1.9 ± 1.3
b_n (H92α)	0.881–0.973	0.997–0.999	0.819–0.887	0.998–0.999
b_n (H53α)	0.70–0.79	0.96–0.98	0.64–0.65	0.97–0.98
β_n (H92α)	−55 ± 32	−1.25 ± 0.75	−70 ± 10	−0.15 ± 0.14
β_n (H53α)	−27 ± 13	−10 ± 3	−13 ± 2	−5 ± 1
$S_{\rm ff,43}$[b] (mJy)	70 ± 30	70 ± 30	19 ± 2	19 ± 2
$N_{\rm Lyc}$ (10^{52} s^{-1})	5 ± 2	5 ± 2	0.9 ± 0.1	0.9 ± 0.1

[a] Both components were used to fit the continuum emission at 8.3 and 43 GHz, as well as the flux densities in the RRLs H92α and H53α.
[b] Free-free continuum flux density at 43 GHz obtained summing the contributions from the low- and high-density components.

The results obtained for the low-density gas component for the NE component of NGC 253 are in agreement with the results obtained by Mohan et al. (2005) for the 15 pc region, observed with higher angular resolution observations (∼0.″3) and using VLA H166α, H92α, and H75α line data. Even though the mass contribution of the high-density H II regions is only ∼1% of the total H II mass, this feature contributes ∼40% of the total H53α line emission.

As noted before by Mohan et al. (2005), high angular resolution observations are essential in the determination of the physical parameters of both low- and high-density H II regions. In addition to high angular resolution, high-frequency observations (e.g., H53α) are required to determine the properties of the high-density (∼10^5 cm^{-3}) H II regions. Non-LTE effects are important, leading to an enhancement of the line emission by a factor of ∼2. Thus, the results obtained assuming LTE conditions overestimate the number of H II regions (and also the SFR) that must exist in NGC 253.

4.2. *Kinematics*

The previous H92α line observations at 1.″8 × 1.″0 angular resolution (Anantharamaiah & Goss 1996) revealed velocity gradients of ∼11 and ∼18 km s^{-1} arcsec^{-1} along the major axis and minor axis, respectively. A qualitative comparison of the velocity field observed in the H53α line and the previously reported H92α line velocity field reveals kinematical behaviors that are consistent; i.e., the regions with redshifted and blueshifted ionized gas coincide (see Figs. 5 and 6). The coincidence of the redshifted and blueshifted regions in the H53α and H92α velocity fields implies that both the low- and high-density ionized gas components rotate in the same sense.

In order to compare in detail the kinematics of the ionized gas as observed in the H53α and H92α lines, we constructed position-velocity (PV) diagrams along the major axis (P.A. = 52°) using the task SLICE in GIPSY. These PV diagrams are shown in Figure 9; the white line is the resulting fit to the velocity gradient of 11 km s^{-1} arcsec^{-1}. The same procedure was used to obtain PV diagrams along the P.A. = −45°, shown in Figure 10; the white lines are the resulting fits to the H92α velocity gradient (24 km s^{-1} arcsec^{-1}) and the H53α velocity gradient (42 km s^{-1} arcsec^{-1}). In Figure 10 we also show the H92α and H53α spectra superimposed at different offset positions from the central source (5.79-39.0); these spectra were normalized based on the peak line flux densities. By inspection of the different spectra obtained at the negative offset positions (between −0.″6 and −0.″9 in Fig. 10), a relative velocity shift (∼30 ± 5 km s^{-1}) is observed between the peak flux density of the H53α and H92α lines. Based on the line emission models,

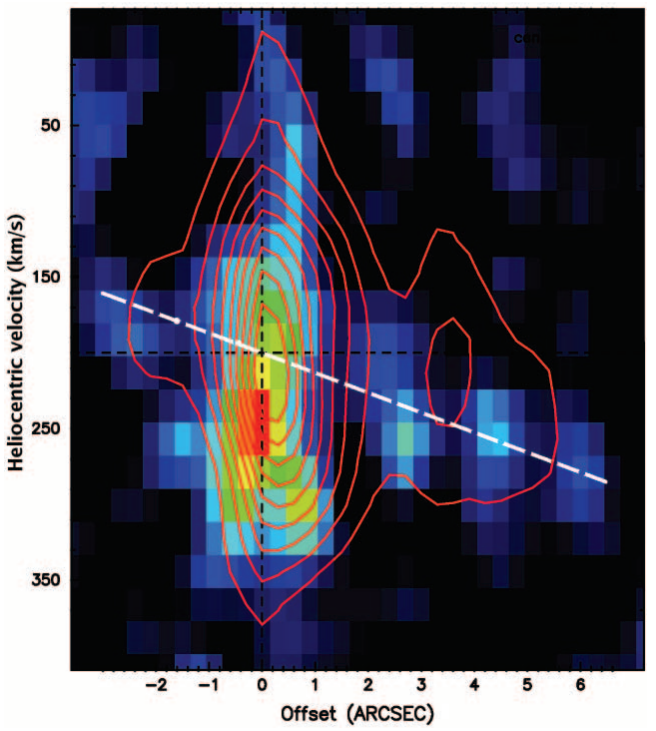

FIG. 9.—PV comparisons along the major axis (P.A. = 52°) of NGC 253. The H53α RRL PV diagram (*color scale*) was constructed from the data with angular resolution of 1.″5 × 1.″0, P.A. = 0° and velocity resolution of 44 km s^{-1}. The color scale covers the range 0.64–6.4 mJy beam^{-1}. The H92α RRL PV diagram (*contours*) was constructed from the data of Anantharamaiah & Goss (1996) with angular resolution of 1.″5 × 1.″0, P.A. = 0° and velocity resolution 56 km s^{-1}. Contours are 10%, 20%, . . . , 90% of the peak intensity 3.9 mJy beam^{-1}. The white dashed line shows the fitted velocity gradient of 11 km s^{-1} arcsec^{-1}.

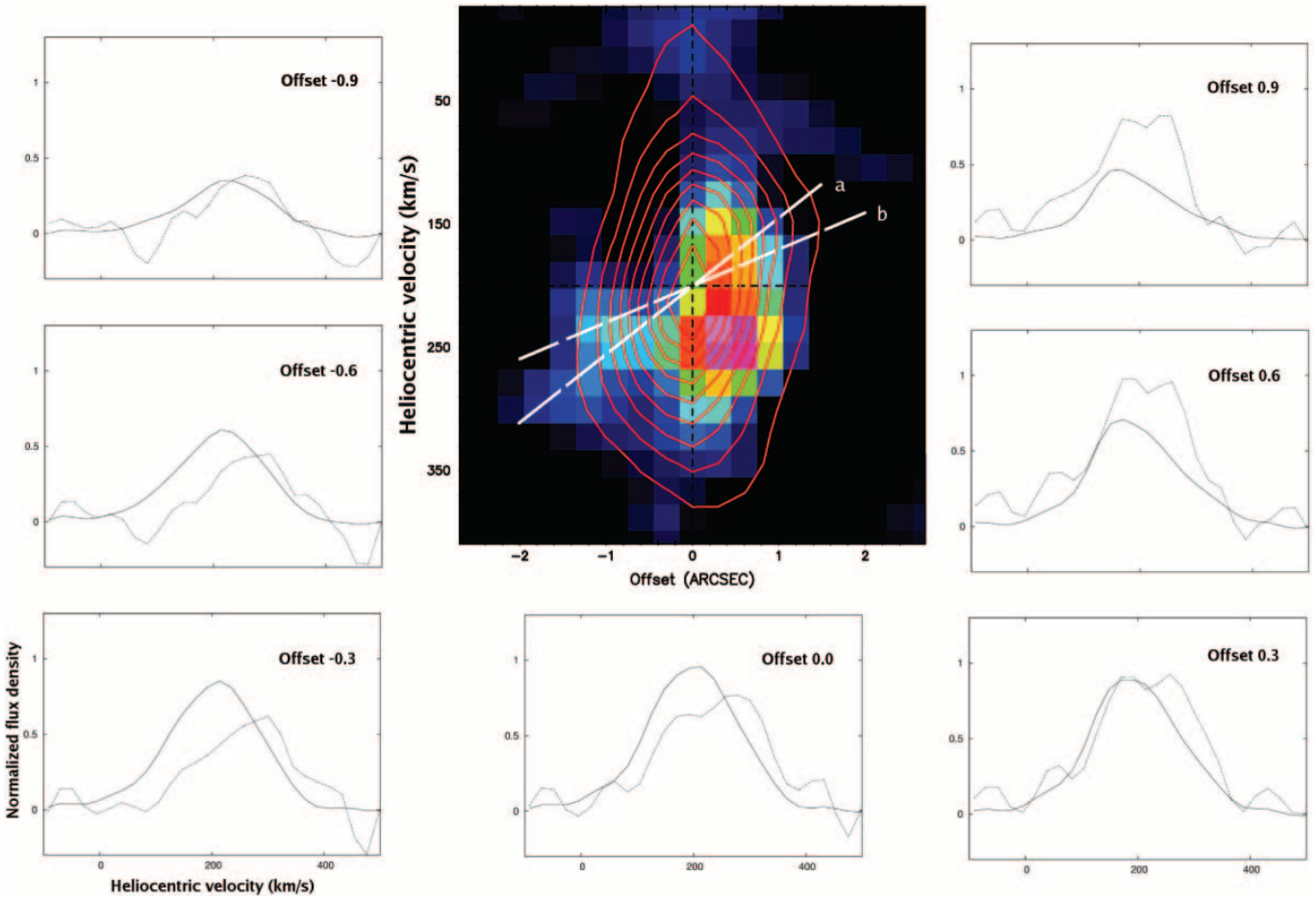

FIG. 10.—PV diagrams along a P.A. = −45° in NGC 253. The H53α RRL PV diagram (*color scale*) was constructed from the data with angular resolution of 1.″5 × 1.″0, P.A. = 0° and velocity resolution of 44 km s^{-1}. The color scale is from 0.64 to 6.4 mJy beam^{-1}. The H92α RRL PV diagram (*contours*) was constructed from the data of Anantharamaiah & Goss (1996), with angular resolution of 1.″5 × 1.″0, P.A. = 0° and velocity resolution of 56 km s^{-1}. Contours are 10%, 20%, . . . , 90% of the peak intensity 3.9 mJy beam^{-1}. The white dashed lines marked with "a" and "b" show the fitted velocity gradients of 42 and 25 km s^{-1} arcsec^{-1}, respectively. The panels show the H53α (*blue*) and H92α (*red*) line profiles for the central 1.″8. Each panel corresponds to a slice taken along the velocity axis of this PV diagram; e.g., the panel at 0.0 is a slice along the velocity axis at offset position 0.″0.

these two RRLs trace different density components (see § 4.1). The small velocity shift between these two RRLs on the NE component suggests that each density component has slightly different kinematics.

4.2.1. *Gaseous Bar Structure, Outflow, or an Accreted Object*

Observations at IR wavelengths have revealed the existence of a gaseous bar in NGC 253 (Scoville et al. 1985). In a bar potential the gas follows two types of orbits, x1 and x2. The x1 (bar) orbits are those extended along the major axis of the bar, and the x2 (antibar) orbits are those oriented perpendicular to the bar major axis. In the case of NGC 253, the x1 and x2 orbits would be oriented on the plane of the sky at P.A. of ∼70° and ∼45°, respectively. In the H53α and H92α RRL images (at 1.″5 × 1.″0 angular resolution) the orientation of the largest velocity gradient is nearly perpendicular to the orientation of the x2 orbits. Since the ionized gas on the NE component rotates in an opposite sense compared to the CO (Anantharamaiah & Goss 1996; Das et al. 2001), a simple bar potential does not account for the differences observed between the velocity fields of the RRLs (H92α and H53α) and CO. A secondary bar inside the primary bar may be invoked to explain the kinematics observed in the center of NGC 253. However, further observations and modeling are required to investigate the existence of this secondary bar.

Weaver et al. (2002) proposed the presence of a starburst-driven nuclear outflow collimated by a dusty torus, based on X-ray observations of NGC 253. In this model, the thermally ionized gas in the center of NGC 253 should be distributed in both a starburst ring and a starburst-driven outflow (Weaver et al. 2002). Observations of the RRL H92α toward the starburst galaxy M82 (Rodríguez-Rico et al. 2004) have proven that RRLs may be used to study the ionized gas associated with galactic outflows. The largest velocity gradient observed in the RRL H92α is oriented nearly along the minor axis of NGC 253 (P.A. = −45°). Based on this orientation and assuming that the H92α RRL in the NE component traces the ionized gas in the outflow, the receding side of this outflow would be on the northwest and the approaching side on the southeast. If this is the case, all of the observed ionized gas would be tracing the outflow, explaining the different rotation sense between the CO and the ionized gas. However, it seems unlikely that all of the ionized gas is associated with the outflow.

Das et al. (2001) propose that the kinematics of the ionized gas traced by the H92α RRL can be explained if there is an accreted object with mass of $\sim 10^6\ M_\odot$. The CO gas that traces the galactic disk of NGC 253 is moving in an opposite sense compared to the ionized gas that may be associated with the compact object. Based on the H53α velocity gradient (∼42 km s^{-1} arcsec^{-1})

along the minor axis of the NE component (~30 pc), the inferred dynamical mass is $\sim 5 \times 10^6\ M_\odot$. This mass estimate is consistent with that of the accreted object proposed by Das et al. (2001). The existence of a compact object is further supported by the higher angular resolution ($0\farcs36 \times 0\farcs21$) H92$\alpha$ observations (Fig. 7), revealing a larger velocity gradient ($\sim$110 km s^{-1} arcsec^{-1}, at P.A. $\simeq -45^\circ$) over the central $\sim 0\farcs6$ (7 pc). This H92α velocity gradient of $\sim$110 km s^{-1} arcsec^{-1} implies a dynamical mass of $\sim 7 \times 10^6\ M_\odot$, similar to the mass determined from the $1\farcs5 \times 1\farcs0$ angular resolution observations of the RRLs H53α and H92α. The $\sim 7 \times 10^6\ M_\odot$ dynamical mass is based on observations over a region a factor of 3 times smaller than that observed in the $1\farcs5 \times 1\farcs0$ angular resolution images.

The estimated dynamical mass ($\sim 7 \times 10^6\ M_\odot$) for the nuclear region of NGC 253 is comparable to that of the compact source at the nucleus of our galaxy ($\sim 4 \times 10^6\ M_\odot$; Ghez et al. 2005). This mass estimate of $\sim 7 \times 10^6\ M_\odot$ for the central region of NGC 253 could exist in the form of a large number of stars combined with ionized gas and may also contain an AGN. If the Lyman continuum photon rate ($\sim 7 \times 10^{52}$ s^{-1}) is mainly due to O5 stars, each emitting $\sim 5 \times 10^{48}$ s^{-1}, then there must be $\sim 10^4$ O5 stars in the NE component. Using Salpeter's IMF and a mass range of 0.1–100 $M_\odot$, the total mass in stars in the NE component is $\sim 10^7\ M_\odot$. The ionized gas could be gravitationally bounded by the stars and consequently the black hole mass would be $\leq 10^7\ M_\odot$. The existence of an AGN has been proposed from radio continuum observations (Turner & Ho 1985; Ulvestad & Antonucci 1997) and RRL H92α observations (Mohan et al. 2002). Radio continuum observations (1.3–20 cm) reveal that the strongest radio source 5.79-39.0 has a brightness temperature >40,000 K at 22 GHz and is unresolved (<1 pc; Ulvestad & Antonucci 1997). Broad (>100 km s^{-1}) H_2O maser line emission is observed toward the nuclear regions, supporting the existence of a massive object in the center of NGC 253 (Nakai et al. 1995).

In order to account for the different kinematics observed for the ionized and the molecular gas, three possible scenarios can be proposed: (1) a dense object that is accreted into the nuclear region of NGC 253, (2) the ionized gas is moving in a starburst-driven outflow, and/or (3) a secondary bar exists within the primary bar, as proposed for other galaxies (Friedli & Martinet 1993). The accreted object model is supported by the high angular resolution H92α observations; the estimated dynamical mass of $\sim 7 \times 10^6\ M_\odot$ is concentrated in a $\leq$7 pc region, and the ionized gas traced by the RRLs moves in the opposite direction compared to the larger scale CO. In the RRLs H53α and H92α, we find no evidence that confirms the existence of a secondary bar. An S shape in the velocity field is characteristic of a bar (Anantharamaiah & Goss 1996). Thus, for a secondary bar a second S-shaped pattern would be observed in the velocity field that is not appreciated in the H92α velocity structure (see Fig. 7). However, this scenario cannot be ruled out, and higher angular and spectral resolution observations are necessary to discern between these three models.

5. CONCLUSIONS

The H53α RRL and radio continuum at 43 GHz were observed at high angular resolution ($1\farcs5 \times 1\farcs0$) toward NGC 253. We have also reanalyzed previous observations of the RRL H92α made at angular resolutions of $1\farcs5 \times 1\farcs0$ (Anantharamaiah & Goss 1996) and $0\farcs36 \times 0\farcs21$ (Mohan et al. 2002).

Based on the 43 GHz radio continuum flux density and previous measurements at lower and higher frequencies, we have estimated the contribution from free-free emission (~140 mJy at 43 GHz). Using this value for the free-free emission, the derived SFR in the nuclear region of NGC 253 is 2 $M_\odot$ yr^{-1}. The RRLs (H53α and H92α) and radio continuum (at 43 and 8.3 GHz) emission have been modeled using a collection of H II regions. Based on the models, the RRL H53α enables us to trace the compact (~0.1 pc) high-density ($\sim 10^5$–10^6 cm^{-3}) H II regions in NGC 253. The total mass of high-density ionized gas in the central 18 pc is $\sim 10^3\ M_\odot$. A large velocity gradient (~42 km s^{-1} arcsec^{-1}, P.A. $\sim -45^\circ$) is observed in the H53α line. The orientation and amplitude of the velocity gradients (angular resolution ~1.″2) derived using the H53α and H92α lines agree. The high angular resolution observations ($0\farcs36 \times 0\farcs21$) of the H92$\alpha$ line reveal a larger velocity gradient (~110 km s^{-1} arcsec^{-1}); this large velocity gradient implies a dynamical mass on the NE component ($\leq$7 pc) of $\sim 7 \times 10^6\ M_\odot$, supporting the existence of an accreted compact object.

The orientation of the H53α and H92α velocity gradients does not agree with the CO kinematics. The different kinematics observed over a larger region of the disk of NGC 253 also suggests the existence of an accreted object. The derived dynamical mass ($\sim 7 \times 10^6\ M_\odot$) can be accounted for by a large stellar density and/or the presence of an AGN. The star formation activity in NGC 253 may be the result of a merger process of NGC 253 and this proposed massive compact object.

The National Radio Astronomy Observatory is a facility of the National Science Foundation operated under cooperative agreement by Associated Universities, Inc. C. A. R.-R. and Y. G. acknowledge support from UNAM and CONACyT, México.

REFERENCES

Anantharamaiah, K. R., & Goss, W. M. 1996, ApJ, 466, L13
Anantharamaiah, K. R., Viallefond, F., Mohan, N. R., Goss, W. M., & Zhao, J. H. 2000, ApJ, 537, 613
Antonucci, R. R. J., & Ulvestad, J. 1988, ApJ, 330, L97
Arnaboldi, M., Capaccioli, M., Cappellaro, E., Held, E. V., & Koribalski, B. 1995, AJ, 110, 199
Boomsma, R., Oosterloo, T. A., Fraternali, F., van der Hulst, J. M., & Sancisi, R. 2005, A&A, 431, 65
Canzian, B., Mundy, L. G., & Scoville, N. Z. 1988, ApJ, 333, 157
Carlstrom, J. E. 1990, in ASP Conf. Ser. 12, The Evolution of the Interstellar Medium, ed. L. Blitz (San Francisco: ASP), 339
Chini, R., Kreysa, E., Mezger, P. G., & Gemuend, H.-P. 1984, A&A, 137, 117
Das, M., Anantharamaiah, K. R., & Yun, M. S. 2001, ApJ, 549, 896
de Vaucouleurs, G., de Vaucouleurs, A., & Corwin, H. G. 1976, Second Reference Catalogue of Bright Galaxies (Austin: Univ. Texas Press)
Engelbracht, C. W., Rieke, M. J., Rieke, G. H., Kelly, D. M., & Achtermann, J. M. 1998, ApJ, 505, 639
Forbes, D. A., & Depoy, D. L. 1992, A&A, 259, 97
Forbes, D. A., Polehampton, E., Stevens, I. R., Brodie, J. P., & Ward, M. J. 2000, MNRAS, 312, 689
Friedli, D., & Martinet, L. 1993, A&A, 277, 27
Krugel, E., Klein, U., Lemke, R., Wielebinski, R., & Zylka, R. 1990, A&A, 240, 232
Mohan, N., Anantharamaiah, K. R., & Goss, W. M. 2002, ApJ, 574, 701
Mohan, N., Goss, W. M., & Anantharamaiah, K. R. 2005, A&A, 432, 1
Nakai, N., Inoue, M., Miyazawa, K., Miyoshi, M., & Hall, P. 1995, PASJ, 47, 771
Paglione, T. A. D., Tosaki, T., & Jackson, J. M. 1995, ApJ, 454, L117
Paglione, T. A. D., Yam, O., Tosaki, T., & Jackson, J. M. 2004, ApJ, 611, 835
Panagia, N. 1973, AJ, 78, 929
Pence, W. D. 1981, ApJ, 247, 473
Peng, R., Zhou, S., Whiteoak, J. B., Lo, K. Y., & Sutton, E. C. 1996, ApJ, 470, 821
Piña, R. K., Jones, B., Puetter, R. C., & Stein, W. A. 1992, ApJ, 401, L75
Prada, F., Gutierrez, C. M., & McKeith, C. D. 1998, ApJ, 495, 765
Puxley, P. J., Mountain, C. M., Brand, P. W. J. L., Moore, T. J. T., & Nakai, N. 1997, ApJ, 485, 143

Rodríguez, L. F., Moran, J. M., Gottlieb, E. W., & Ho, P. T. P. 1980, ApJ, 235, 845
Rodríguez-Rico, C. A., Viallefond, F., Zhao, J. H., Goss, W. M., & Anantharamaiah, K. R. 2004, ApJ, 616, 783
Schraml, J., & Mezger, P. G. 1969, ApJ, 156, 269
Scoville, N. Z., Soifer, B. T., Neugebauer, G., Matthews, K., Young, J. S., & Yerka, J. 1985, ApJ, 289, 129
Turner, J. L., & Ho, P. T. P. 1983, ApJ, 268, L79
———. 1985, ApJ, 299, L77
Ulvestad, J., & Antonucci, R. R. J. 1997, ApJ, 488, 621
Weaver, K. A., Heckman, T. M., Strickland, D. K., & Dahlem, M. 2002, ApJ, 576, L19